Supplementary Information (SI) for Green Chemistry.

Supporting information

Dual Modulation of Electronic and Crystalline Structures in PtCo Alloys for High-Performance Fuel Cells

Si Lin[a,+], Ziyu Zhang[a,+], Yunlong Zhang[a,*], Yunfei Xia[a], Miao Ma[a], Lixiao Shen[a,b], Xin Wang[a,b], Shengdi Tian[a], Zigang Zhao[a], Wen Ye[a], Aibin Chen[c,*], Xiaofei Gong[d,*], Lei Zhao[a,*], Zhenbo Wang[a, b, *]

a MIIT Key Laboratory of Critical Materials Technology for New Energy Conversion and Storage, State Key Lab of Urban Water Resource and Environment, School of Chemistry and Chemical Engineering Harbin Institute of Technology, Harbin 150001, P. R. China

b College of Materials Science and Engineering, Shenzhen University, Shenzhen 518071, China.

c College of Chemical and Pharmaceutical Engineering, Hebei University of Science and Technology, 26 Yuxiang Street, Shijiazhuang 050018, P.R. China.

d School of Marine Science and Technology, Harbin Institute of Technology at Weihai, 2 West Wenhua Road, Weihai 264209, China.

* Corresponding authors E-mail addresses: zhangyunlong@hit.edu.cn; chen_ab@163.com; gongxf@hit.edu.cn; leizhao@hit.edu.cn; wangzhb@hit.edu.cn (Lead Contact).

Experimental Section

Chemicals:

Cobalt nitrate hexahydrate ($Co(NO_3)_2 \cdot 6H_2O$) and chloroplatinic acid hexahydrate ($H_2PtCl_6 \cdot 6H_2O$) were purchased from Shanghai Aladdin Biochemical Technology Co., Ltd. Polyvinylpyrrolidone (PVP) was obtained from Shanghai Yuanye Bio-Technology Co., Ltd. Anhydrous ethanol (CH_3CH_2OH) and anhydrous isopropanol ($(CH_3)_2CHOH$) were supplied by Tianjin Tianli Chemical Reagent Co., Ltd. Perchloric acid ($HClO_4$) was acquired from Tianjin Comio Chemical Co., Ltd. The carbon support (Ketjen Black EC-300J) was procured from Japan. Nafion solutions (5 wt% and 60 wt%) were provided by DuPont, and commercial platinum/carbon catalyst (20 wt% Pt/C) was sourced from **Hycatalyst** (Shanghai) Co., Ltd. Deionized water (resistivity 18.2 MΩ·cm) used in all experiments was purified through an ultrapure water system. All chemicals and reagents were used as received without further purification.

Materials Characterization:

The morphological and microstructural features of the carbon support and as-synthesized catalysts were examined by transmission electron microscopy (TEM) using a Tecnai G2 F30 instrument. High-resolution TEM (HRTEM) imaging, elemental mapping, and high-angle annular dark-field scanning TEM (HAADF-STEM) analysis were also conducted to further elucidate the structural and compositional characteristics. The crystalline phases present in the catalysts were identified by powder X-ray diffraction (XRD) on a Bruker D8 diffractometer with Cu $K\alpha_1$ radiation. Raman spectroscopy was performed using a inVia-Reflex system equipped with a 532 nm laser source to probe the carbon structure and defect-related features. Surface chemical composition, bonding states, and elemental binding energies were analyzed by X-ray photoelectron spectroscopy (XPS) on an ESCALAB 250Xi spectrometer. Furthermore, the actual Pt and Co loadings were quantitatively determined by inductively coupled plasma optical emission spectrometry (ICP-OES) using an iCAP 7400 instrument. X-ray Absorption Spectroscopy (XAS) measurements at the Pt L-edge were conducted at the XAS beamline of the Australian Synchrotron (ANSTO), with energy calibration performed using the corresponding metal foil reference. All spectra were collected under ambient conditions (data collection also covered the metal K-edge). For concentrated samples, the catalyst was mounted on a sample holder at a 90° (or 45°) angle relative to the incident beam, and the transmission signal was detected using ionization chambers coupled with a Lytle detector. Data processing included background subtraction and normalization using Athena, followed by EXAFS fitting and analysis performed with Artemis and IFEFFIT software packages.

Electrochemical Measurements:

The electrocatalytic performance of the catalysts was evaluated using a rotating disk electrode (RDE) setup (CHI 760e) in a three-electrode cell with 0.1 M $HClO_4$ as the electrolyte at 25 °C. A catalyst ink was prepared by dispersing 2.5 mg of catalyst in a mixture of 0.3 mL deionized water, 0.67 mL ethanol, and 0.03 mL of 5 wt% Nafion solution, followed by ultrasonication for 40 min; 20 μL of the resulting ink was then drop-cast onto a pre-polished glassy carbon electrode (GCE, 5.61 mm diameter) to achieve a uniform Pt loading of 20 μg_{Pt} cm^{-2}, which served as the working electrode (WE), with a carbon rod as the counter electrode (CE) and a mercury/mercury sulfate electrode (MSE) as the reference electrode (RE). All reported potentials were calibrated to the reversible hydrogen electrode (RHE) scale. For activation and testing under N_2 saturation, the working electrode was first activated by cyclic voltammetry (CV) in N_2-saturated 0.1 M $HClO_4$ between 0.05 and 1.05 V vs. RHE at 100 mV s^{-1} for 40 cycles, followed by N_2 CV scans (50 mV s^{-1}, 6 cycles) and N_2 linear sweep voltammetry (LSV) measurements (quiet time 60 s, 1.05-0.05 V vs. RHE, 10 mV s^{-1}, 0.1 mV sampling interval, 1600 rpm). For oxygen reduction reaction (ORR) tests, the electrode was transferred to an O_2-saturated 0.1 M $HClO_4$ electrolyte, where O_2 activation and O_2 CV were conducted to ensure stability, after which O_2 LSV was recorded under identical conditions as the N_2 LSV, while the ring potential was held at 1.20 V vs. RHE to monitor hydrogen peroxide (H_2O_2) formation. Catalyst stability was assessed via accelerated stress testing (AST) involving 30,000 cycles of CV between 0.60 and 1.00 V vs. RHE at 200 mV s^{-1} in O_2 atmosphere, with N_2 and O_2 LSV measurements repeated every 10,000 cycles. The mass activity (MA) at 0.9 V, electrochemical surface area (ECSA), specific activity (SA), and H_2O_2 yield were calculated using the following expressions:

$$1/jA = 1/jk + 1/jL,$$

$$MA = jk/mPt,$$

$$ECSA = QH/(CDH,UPD \times mPt),$$

$$SA = MA/ECSA,$$

$$H2O2\% = 200 \times Jr/(Jr + N \times Jd)\%,$$

where j_A is the apparent current density (mA cm^{-2}) at 0.9 V, j_K is the kinetic current density (mA cm^{-2}) at 0.9 V, j_L is the limiting current density (mA cm^{-2}) at 0.4 V, m_{Pt} is the Pt mass loading (μg_{Pt} cm^{-2}), QH is the Faradaic charge (μC) integrated in the hydrogen adsorption/desorption region (0.05-0.40 V), CDH,UPD is the charge density for hydrogen adsorption on polycrystalline Pt (210 μC cm^{-2}), J_r and J_d are the ring and disk currents (mA), respectively, and N is the collection efficiency of the RRDE (37%).

Assembly of the Membrane Electrode:

During the assembly of the membrane electrode assembly (MEA), the gas diffusion layer (GDL) used was Toray XGL055, with a thickness of approximately 160 μm under no compression. During assembly, a torque wrench was used to apply torques sequentially at 10 N·m, 20 N·m, 30 N·m, and 40 N·m, holding each torque for 30 seconds, with a final locking torque of 40 N·m. The flow field employed was a single serpentine channel, with a channel width of 0.8 mm, a channel depth of 1.02 mm, and the number of serpentine channels was 1.

Density Functional Theory Calculations:

All density functional theory (DFT) calculations were performed using the Vienna Ab Initio Simulation Package (VASP)[1-3] with the projector augmented-wave (PAW) pseudopotential to describe core electrons[4,5] and the Perdew-Burke-Ernzerhof (PBE) functional within the generalized gradient approximation (GGA) to treat exchange-correlation energy[6]; a vacuum layer larger than 15 Å was applied along the z-direction to avoid spurious interactions between periodic slabs, while a plane-wave cutoff energy of 400 eV was adopted and Brillouin zone integration was sampled with a 1×1×1 Monkhorst-Pack k-point grid[7], where the self-consistent field (SCF) calculations were converged to 10^{-5} eV and the maximum force on each atom was less than 0.02 eV/Å. The DM-$L1_0$-PtCoN (111) surface was modeled using a 4×4 in-plane supercell by inserting N atoms into the octahedral interstitial sites of the top two atomic layers, and in all calculations the bottom two layers of both DM-L10-PtCoN (111) and UM-PtCo (111) models were fixed while the top two layers were fully relaxed. The vacancy formation energy was evaluated as

$$V(M) = E(slab - M) + \mu(M) - E(slab),$$

where E(slab-M) and E(slab) denote the total energies of the slab with a metal vacancy and the perfect slab, respectively, and μ(M) represents the chemical potential of a single metal atom in the bulk M crystal.

The oxygen reduction reaction (ORR) was considered to follow a four-electron pathway:

(i) $* + O_2 + H^+ + e^- \rightarrow *OOH$,

(ii) $*OOH + H^+ + e^- \rightarrow *O + H_2O$,

(iii) $*O + H^+ + e^- \rightarrow *OH$,

(iv) $*OH + H^+ + e^- \rightarrow * + H_2O$,

where * denotes an adsorption site. The change in Gibbs free energy (ΔG) was calculated according to

$$\Delta G = \Delta E + \Delta EZPE + \int CPdT - T\Delta S + \Delta GU + \Delta GpH^{8},$$

in which ΔE is the reaction energy change, ΔEZPE the change in zero-point energy, T the temperature (298.15 K), C_P the constant-pressure heat capacity, ΔS the entropy change between products and reactants at temperature T, ΔG_U the contribution of the applied electrode potential U, and ΔG_{pH} the correction due to variation in H^+ concentration; the Gibbs free energy of slab* + $2H_2O$ was taken as the baseline (0 eV) in all models.

Supplementary Figures

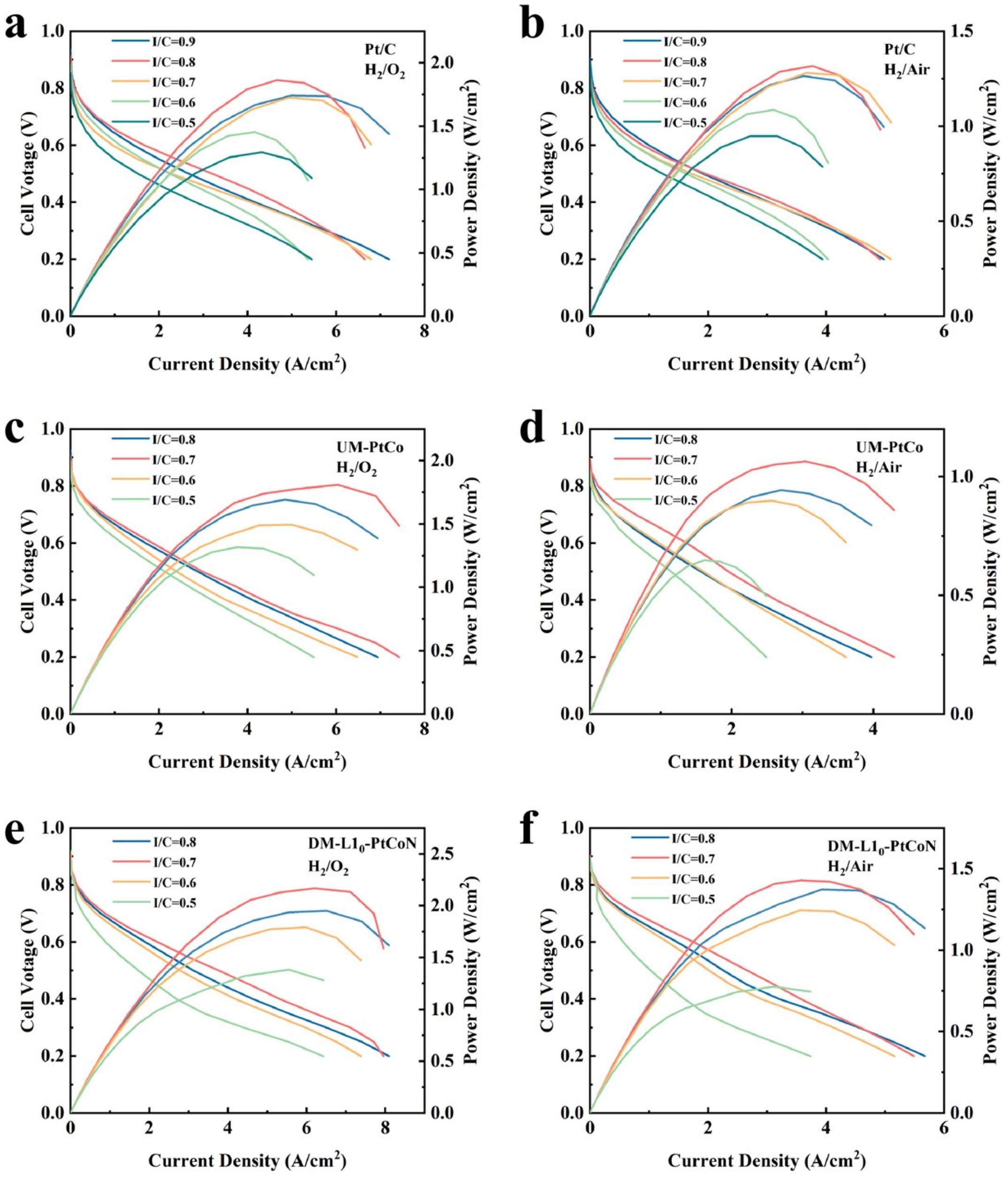

Figure S1. Polarization curves of different catalysts under various I/C ratios: Pt/C: (a) H_2-O_2, (b) H_2-Air; UM-PtCo: (c) H_2-O_2, (d) H_2-Air; DM-L10-PtCo: (e) H_2-O_2, (f) H_2-Air

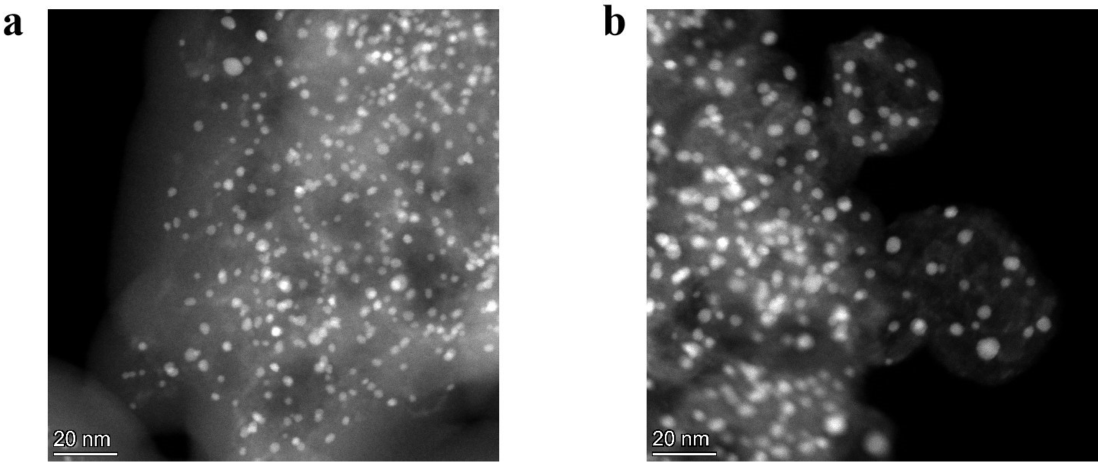

Figure S2. HAADF-STEM image: (a) DM-$L1_0$-PtCoN; (b) UM-PtCo

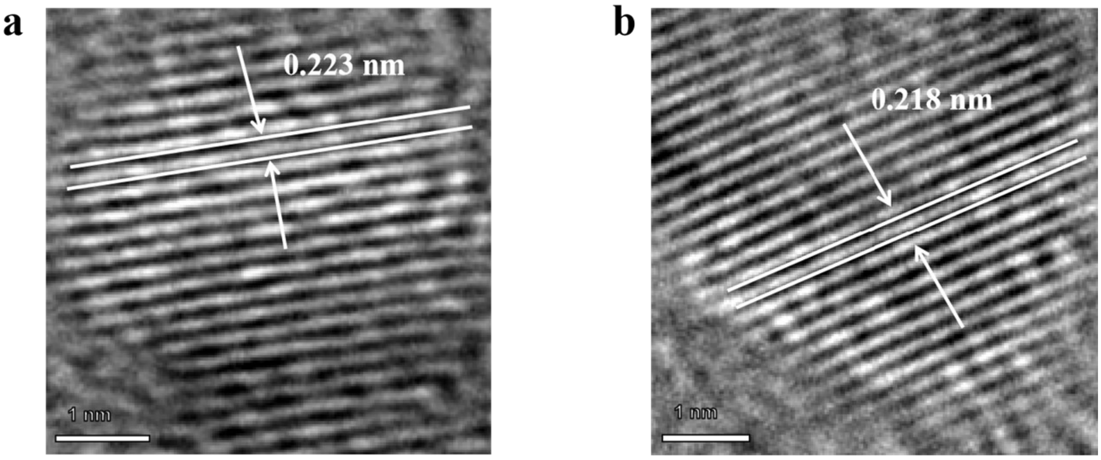

Figure S3. Lattice fringe images of (a) DM-L1_0-PtCoN; (b) UM-PtCo

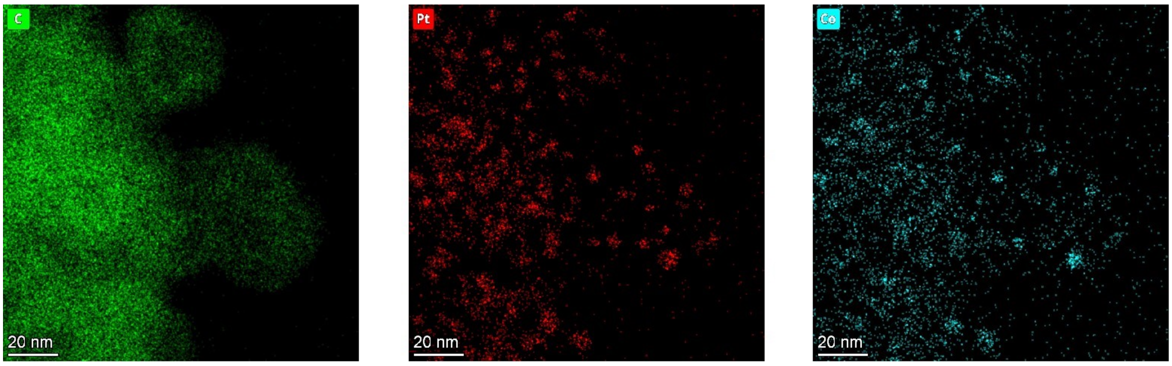

Figure S4. The elemental mapping of the UM-PtCo alloy nanoparticles.

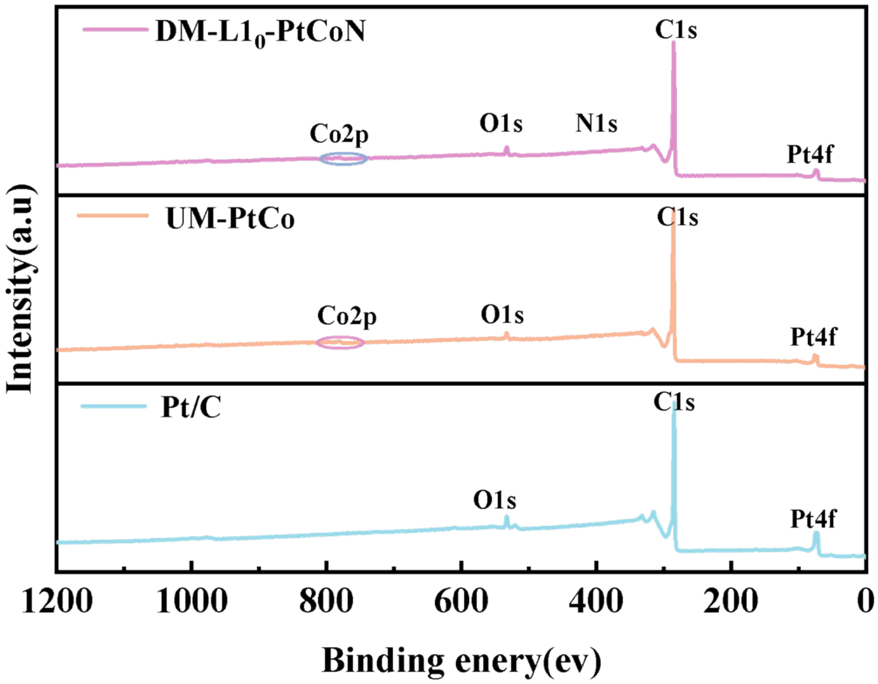

Figure S5. XPS survey spectra of DM-L1$_0$-PtCoN, UM-PtCo and Pt/C.

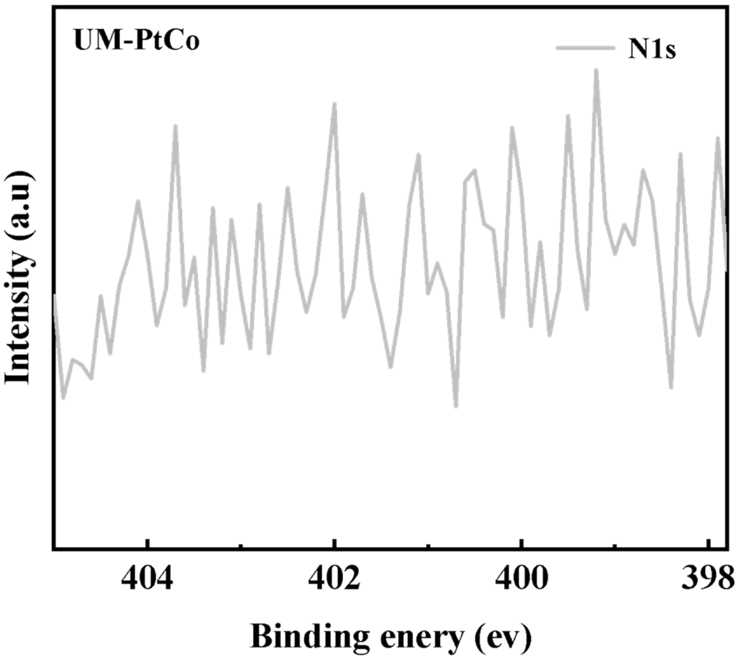

Figure S6. XPS analysis of N 1*s* for UM-PtCo.

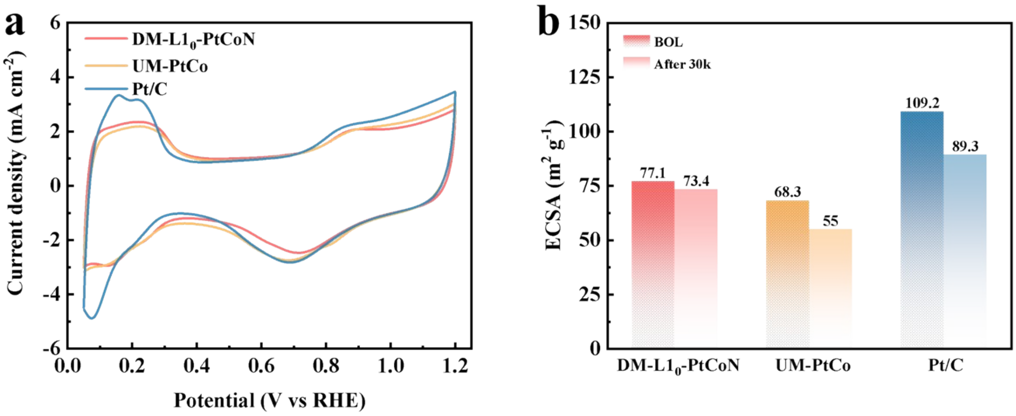

Figure S7. (a) the CV curves of the DM-L1$_0$-PtCoN, UM-PtCo, and Pt/C catalysts, and (b) a performance comparison of their ECSA.

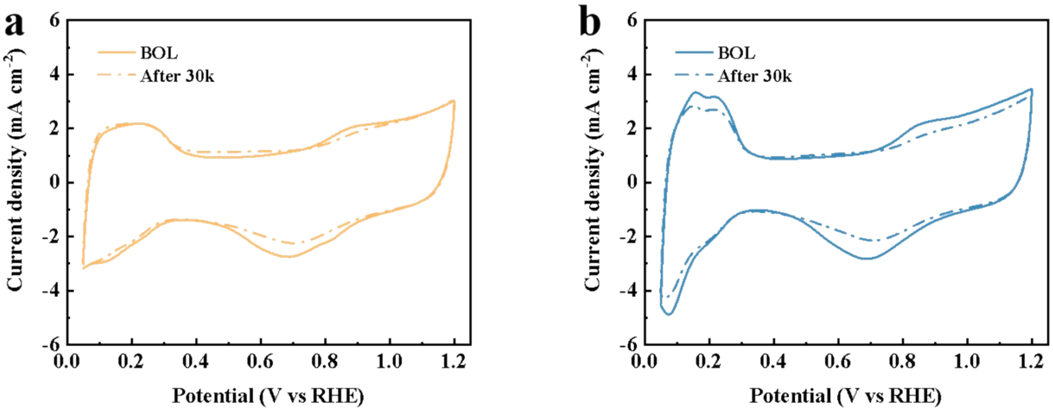

Figure S8. CV curves of (a) UM-PtCo and (b) Pt/C before and after 30,000 AST cycles.

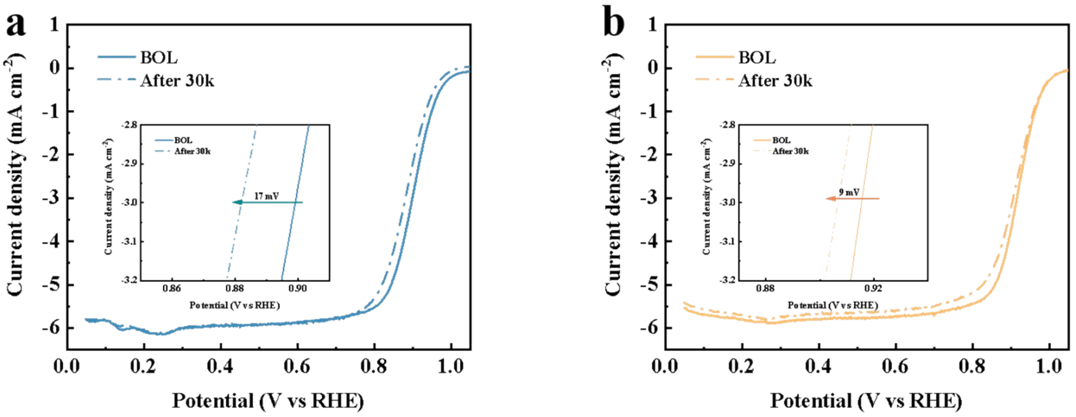

Figure S9. The ORR polarization curves for (a) UM-PtCo and (b) Pt/C, recorded before and after 30,000 AST cycles.

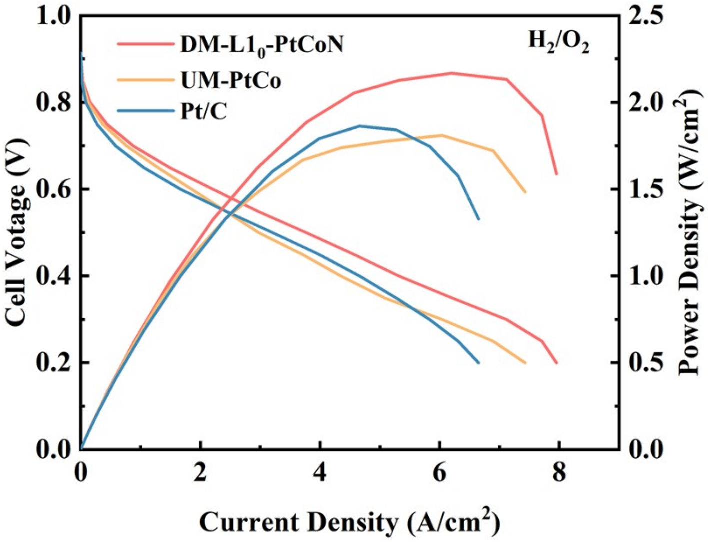

Figure S10. Polarization and power density curves of DM-L1$_0$-PtCoN, UM-PtCo and Pt/C under H_2-O_2 conditions.

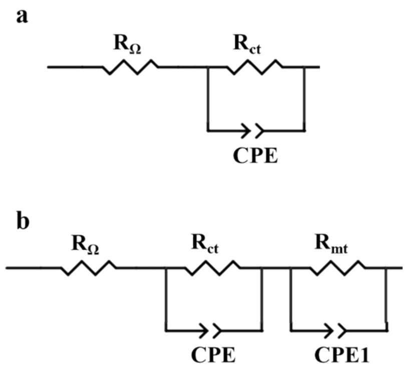

Figure S11. Equivalent circuits of obtained Nyquist plots of (a) DM-L1_0-PtCoN and (b) UM-PtCo.

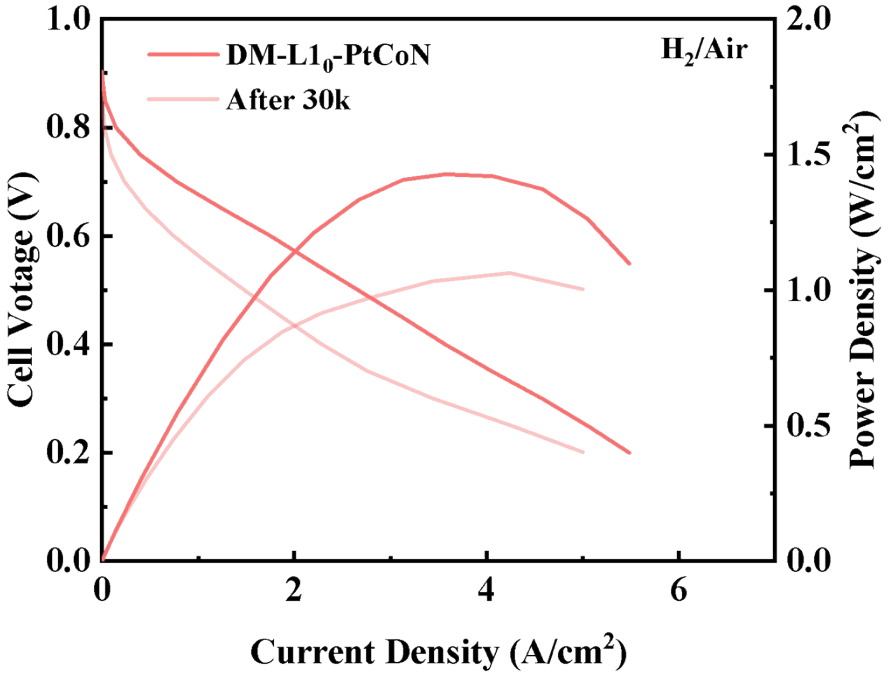

Figure S12. DM-L1$_0$-PtCoN catalyst before and after 30,000 AST cycles under H_2-air conditions.

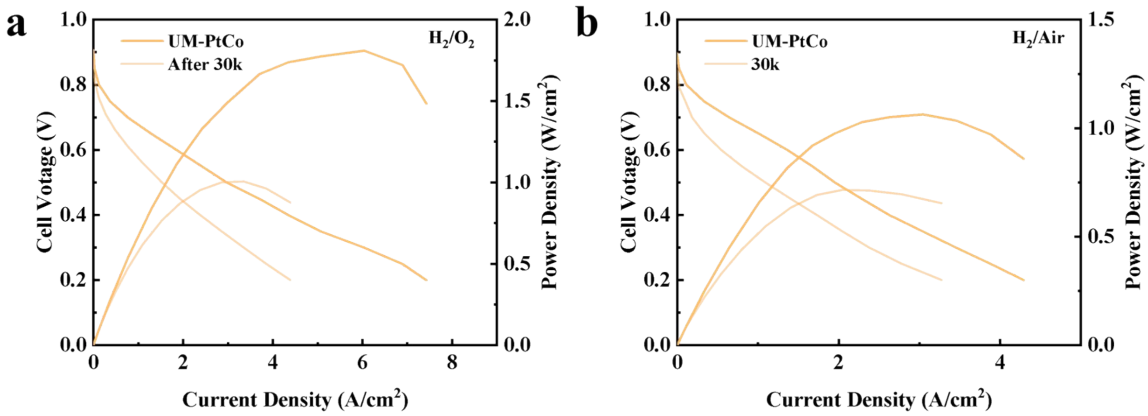

Figure S13. UM-PtCo catalyst before and after 30,000 AST cycles under (a) H_2-O_2 and (b) H_2-air conditions.

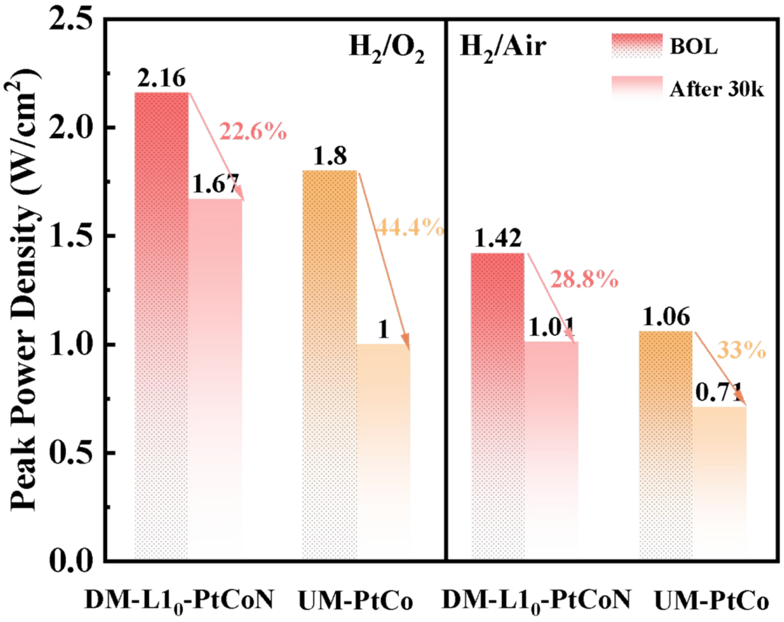

Figure S14. Comparison of peak power density retention after AST for DM-$L1_0$-PtCoN and UM-PtCo.

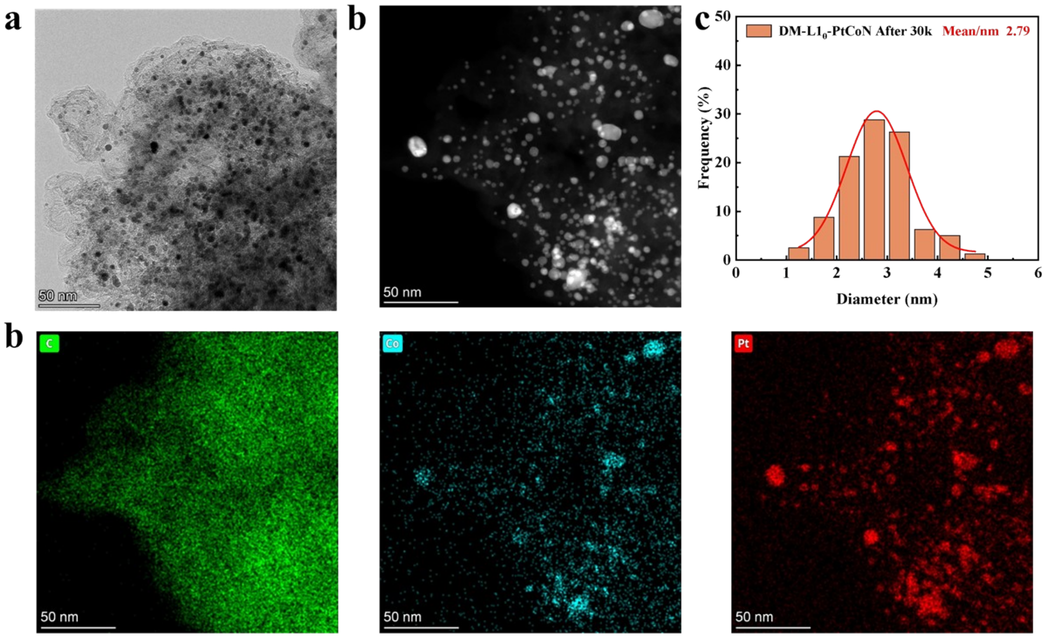

Figure S15. Presents the post-AST characterization of the DM-L1_0-PtCoN catalyst after 30,000 cycles: (a) TEM image; (b) HAADF-STEM image; (c) particle size distribution histogram; and (d) EDS.

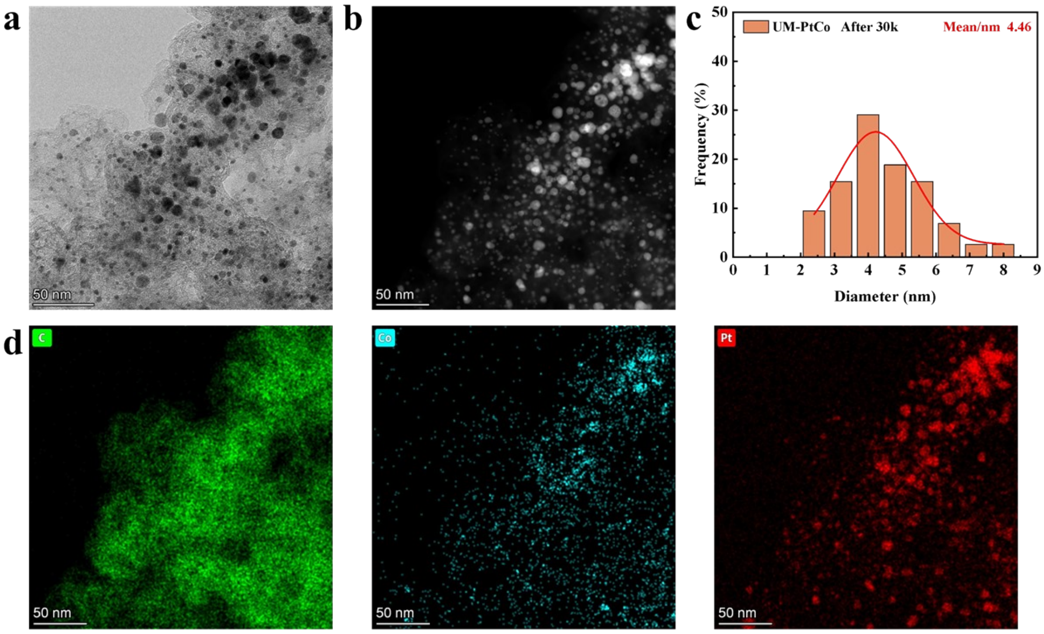

Figure S16. Presents the post-AST characterization of the UM-PtCo catalyst after 30,000 cycles: (a) TEM image; (b) HAADF-STEM image; (c) particle size distribution histogram; and (d) EDS.

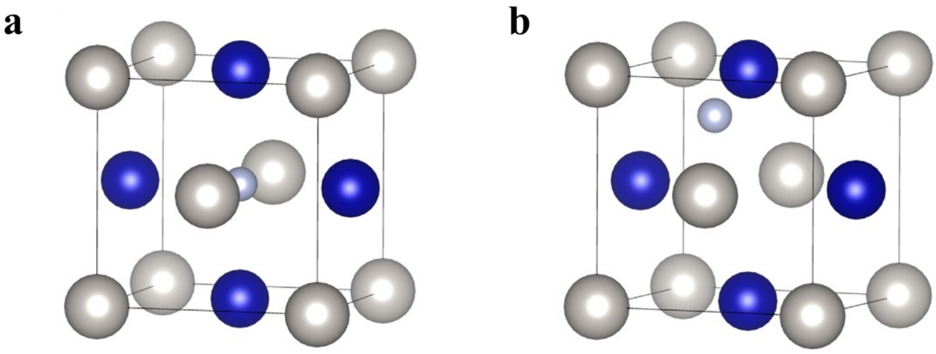

Octahedral **Tetrahedral**

Figure S17. DFT models of different doping sites

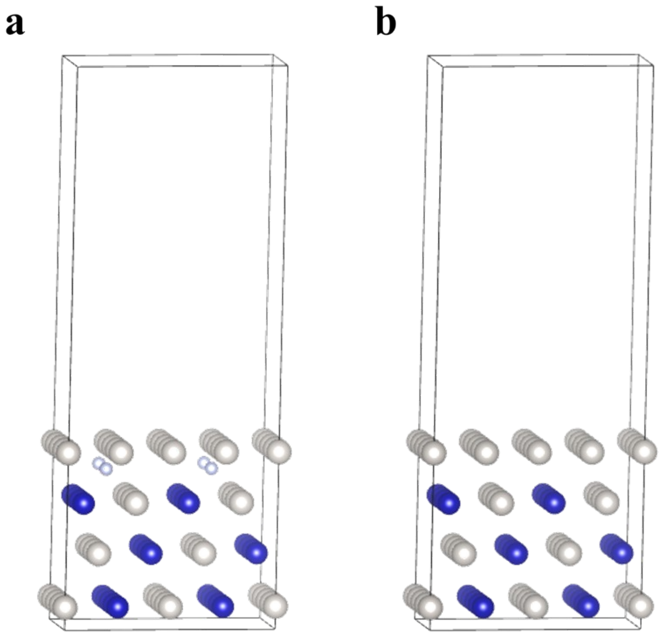

Figure S18. DFT calculation model of (a) DM-L1$_0$-PtCoN and; (b) UM-PtCo.

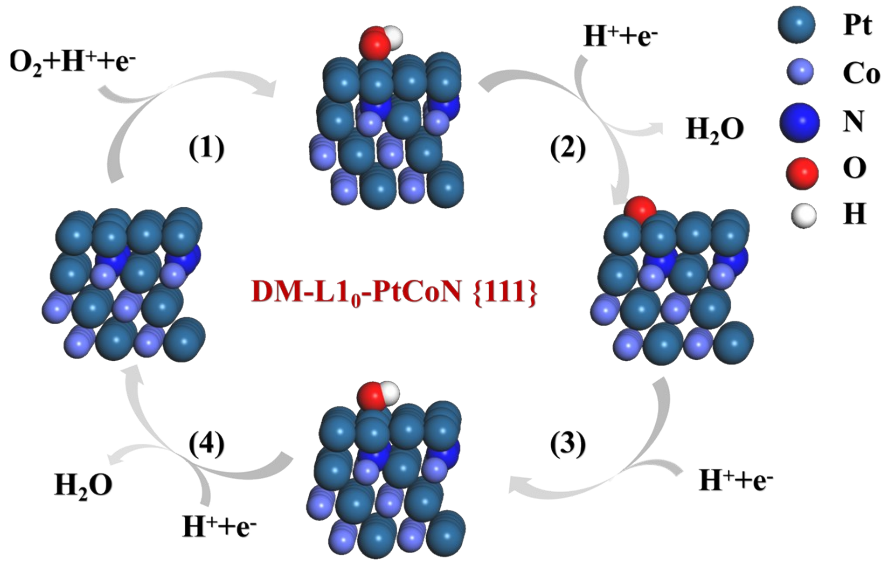

Figure S19. ORR reaction pathway on the DM-L1_0-PtCoN model.

Table S1. Elemental composition analysis of the as-synthesized catalysts determined by ICP-OES.

Sample	**Pt (wt%)**	**Co (wt%)**
DM-L1_0-PtCoN	15.23	2.39
UM-PtCo	17.00	4.13
Pt/C	22.59	-

Table S2. Current densities of different catalysts at various potentials

Catalysis	**Current density at 0.8 V (A cm^{-2})**		**Current density at 0.6 V (A cm^{-2})**	
	H_2-O_2	H_2-Air	H_2-O_2	H_2-Air
DM-L1_0-PtCoN	0.15	0.14	2.21	1.75
UM-PtCo	0.12	0.11	1.85	1.36
Pt/C	0.08	0.04	1.66	0.88

Table S3. Comparison of Peak Power Densities under H_2-O_2/H_2-Air Conditions in fuel cells

Catalysts	**Anode/Cathode Pt Loading**	**H_2/O_2 Flow Rate(slm）-Pressure Relationship（kpa）**	**H_2/Air Flow Rate(slm）- Pressure Relationship（kpa）**	**Peak Power Densities under H_2-O_2/H_2-Air Conditions（W/cm^2）**	**References**
DM-L1_0-PtCoN	0.1/0.1	0.5/0.5-100	0.5/2-180	2.16/1.42	This work
H-PtCo NDs	0.1/0.05	0.3/0.8-250	0.3/0.8-250	1.76/0.75	https://doi.org/10.1016/j.jechem.2025.04.007
PtCoV-EPNF	0.1/0.06	0.4/0.4-200	0.3/0.5-200	1.74/0.80	https://doi.org/10.1002/adma.202502457
L10-PtCoIn@Pt	0.1/0.1	0.5/1-250	0.5/1-250	1.99/0.99	https://doi.org/10.1002/anie.202501805
Pt-B/C	0.12/0.12	150	150	1.60/0.80	https://doi.org/10.1021/acscatal.2c01052
Pt$_3$FeCo	0.1/0.05	0.5/1-150	0.5/1-150	1.80/0.90	https://doi.org/10.1002/adma.202208672
HEI@Pt/C	0.1/0.1	0.4/1-150	1/1-150	2.44/0.96	https://doi.org/10.1002/adfm.202503628
Pt$_{54}$Pd$_{46}$/B-C	0.025/0.1	0.6/0.6-20	0.6/1-200	2.33/1.04	https://doi.org/10.1021/acsami.2c08510
Zn-NC-Ar-PtZn	0.1/0.1	0.5/0.5-100	0.5/2-150	1.48/1.04	https://doi.org/10.1016/j.jcat.2024.115296.

Table S4. EIS analysis of the MEAs measured of DM-L1_0-PtCoN and UM-PtCo in H_2/O_2 at 0.65 V

Sample	**R_Ω (Ω cm^2)**	**R_{ct} (Ω cm^2)**
DM-L1_0-PtCoN	0.037	0.075
UM-PtCo	0.046	0.093

Table S5. Formation energies for different doping sites

Doping site	Formation energy (eV)
Octahedral	-33.43
Tetrahedral	-33.08

References

1 G. Kresse, and J. Furthmuller, *Comput. Mater. Sci.*, 1996, **6**, 15-50, https://doi.org/10.1016/0927-0256(96)00008-0.

2 J.K. Nørskov, J. Rossmeisl, A. Logadottir, L. Lindqvist, J.R. Kitchin, T. Bligaard, and H. Jónsson, *J. Phys. Chem. B*, 2004, **108**, 17886-17892, https://doi.org/10.1021/jp047349j.

3 V. Viswanathan, H.A. Hansen, J. Rossmeisl, and J.K. Nørskov, *ACS Catal.,* 2012, **2**, 1654-1660, https://doi.org/10.1021/cs300227s.

4 D. Vanderbilt, *Phys. Rev. B*, 1990, **41**, 7892-7895.

5 P.E. Blöchl, *Phys. Rev. B*, 1994, **50**, 17953-17979.

6 J.P. Perdew, K. Burke, and M. Ernzerhof, *Phys. Rev. Lett.*, 1996, **77**, 3865-3868.

7 S. Froyen, *Phys. Rev. B*, 1989, **39**, 3168-3172, https://doi.org/10.1103/PhysRevB.39.3168.

8 S. Zaman, Y.-Q. Su, C.-L. Dong, R. Qi, L. Huang, Y. Qin, Y.-C. Huang, F.-M. Li, B. You, W. Guo, Q. Li, S. Ding, and B.-Y. Xia, *Angew. Chem. Int. Ed.*, 2022, **61**, e202115835-e202115843, https://doi.org/10.1002/anie.202115835.